INTERNATIONAL JOURNAL FOR NUMERICAL METHODS IN FLUIDS, VOL. 14, 459–475 (1992)

NUMERICAL SIMULATION OF TWIN-JET IMPINGEMENT ON A FLAT PLATE COUPLED WITH CROSS-FLOW

SHU-HAO CHUANG

Department of Mechanical Engineering, National Chung-Hsing University, Taichung, Taiwan 40227, R.O.C.

MING-HUA CHEN

Chung-Chou Institute of Technology, Changhua, Taiwan 51022, R.O.C.

SHEN-WU LII

Department of Applied Mathematics, National Chung-Hsing University, Taichung, Taiwan 40227, R.O.C.

AND

FANG-MEI TAI

Department of Industrial Engineering and Management, Shu-Teh Junior College of Technology, Taichung, Taiwan 40202, R.O.C.

SUMMARY

Theoretical research to simulate twin-jet impingement with cross-flow has been undertaken. An impinging twin jet coupled with cross–flow in closed ground effect has been studied by using the compressible Navier–Stokes equation with a Jones–Launder k–ε two-equation turbulence model. The velocity results without cross-flow were compared with the data of Saripalli *et al.* and found to show good agreement. The calculated results show that several recirculating zones are distributed around the flow field. Their size and location are closely related to the jet exit height above the ground, the nozzle space and the strength of cross-flow. In addition, a fountain upwash flow occurs between the nozzles, and two low-pressure recirculating zones are induced by the interaction between the nozzle mainstream and the fountain upwash flow. This induce a loss of lift force of the aircraft. The effects of the cross-flow induce the sudden decrease in the lift force of the aircraft; the stronger the cross-flow, the lower is the lift force of the flow field.

KEY WORDS Impinging twin jet Fountain upwash flow Cross-flow Lift force k–ε model

INTRODUCTION

Current advanced fighter aircraft are designed for high manoeuvrability over a wide range of Mach numbers and engine power settings; the interest in jet- and fan-powered vertical/short-take-off-and-landing (V/STOL) military aircraft will increase in the near future. Over the last 20 years numerous analytical and experimental studies of propulsion induced by aerodynamic effects have been performed in an effort to provide practical prediction methods for a range of aircraft configurations and operating conditions.

Quite a lot of studies have concentrated on the hover mode of VTOL flight, in which the suck-down, fountain formation, and hot gas ingestion resulting from the induced flows and interaction of the lift jets and the cross-flow are not fully understood. These lift systems induced

0271–2091/92/040459–17$08.50

Received November 1990
Revised June 1991

by aerodynamic effects cannot be easily predicted either theoretically or from scaled experiments. The numerous variables which affect the flow field make it costly to study an aircraft configuration through wind-tunnel tests. In order to gain a fundamental understanding of a less complex lift-jet-induced flow theoretical research to simulate the impinging twin jet with cross-flow has been undertaken.

The impinging twin-jet flow treated in the present paper is shown schematically in Figures 1 and 2. It can be characterized by the following regions: (a) the free jet region in which the flow is essentially the same as that of a jet issuing into an unbounded region of the same fluid; (b) the impingement region in which the flow changes direction with a large pressure gradient; (c) the wall jet region in which the flow spreads over the ground surface with zero pressure gradient; (d) the fountain upwash region which is produced by the inward-colliding wall jet; (e) the entrainment region in which the flow is ambient air into the different regions of the flow. Wolfshtein[1] summarized all experimental and analytic studies of the planar turbulent impinging jet up to 1970 in his review paper. Experimental measurements of the impinging jet with a round nozzle were carried out by Coleman,[2] who found that the flow was essentially characterized by three regions, namely the free jet region, the jet impingement region and the wall jet region. The static pressure distribution of the ground plane for the impinging region has been solved by the frozen vorticity concept.[3] Theoretical analyses of impinging jet flow have been concerned with finding solutions of several separate regions and then combining these into a complete solution.[4,5] The two-dimensional Navier–Stokes equation with ground effect was studied by Bower and Kotansky,[6] who first utilized the augmented central difference and one-equation turbulent model to simulate the impinging jet flow. Two- and three-dimensional impinging jet flow was studied by Bower and co-workers,[7–9] who utilized the streamfunction–vorticity and Jones–Launder[10] k–ε two-equation turbulence model. These results showed good agreement between numerical predictions and experimental data. Incompressible, inviscid, rotational impingement problems have also been considered.[11] The results for two-dimensional normal axisymmetric impingement and oblique impingement jets compared well with the experimental data of Rubel.[11] Agarwal and Bower[12] and Looney and Walsh[13] used the same turbulence model to predict the impinging jet flow and found similar agreement. The above solution methods were limited to the use of streamfunction–vorticity for solving the Navier–Stokes equations. Ho and Nosseir investigated the feedback phenomenon in an impinging jet.[14] They found that pressure fluctuations were generated by the impingement of the coherent structures on the plate. These pressure fluctuations propagate upstream and form a feedback loop with the downstream-convected coherent structure. The upstream-propagating pressure waves excite the thin shear layer near the nozzle lip and produce a periodic coherent structure. Besides, these pressure

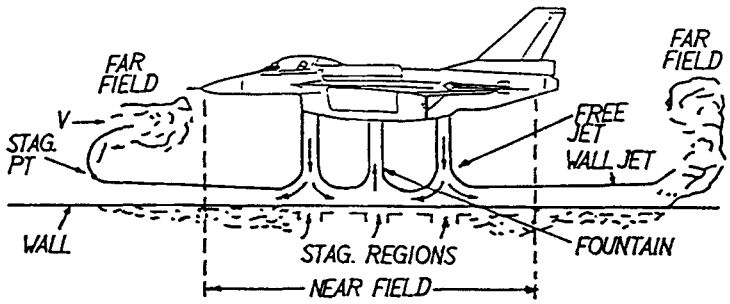

Figure 1. VTOL military aircraft

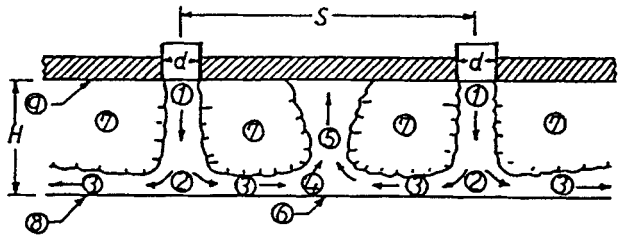

1. Lift jet flow
2. Jet impingement region
3. Wall jet flow
4. Fountain formation region
5. Fountain up-wash flow
6. Wall jet interaction stagnation line
7. Entrainment
8. Ground plane
9. Upper surface

Figure 2. Impinging twin jet

fluctuations will induce self-sustained oscillation in some situations.[15,16] Ho and Hsiao[17] employed an experimental method to study the interaction between the free shear layer and the boundary layer of the wall jet. In order to further understand the structure of impinging jet flow, one needs to use the primitive variables for solving an impinging twin jet with cross-flow. In viscous flow the fine mesh spacing makes the MacCormack scheme with the explicit method[18,19] extremely costly. Implicit methods[20,21] make use of a possible large time step but require the inversion of block tridiagonal matrices. Numerical simulation of impinging jet flow by the Beam–Warming method[20] has been done by Hwang and Liu.[22] A method developed by MacCormack[23] has eliminated this disadvantage by introducing a predictor–corrector scheme. Unfortunately, this method was demonstrated only for a simple case. There are some studies[24,25] of impinging single-jet flow showing good agreement between numerical predictions and experimental data.

This paper adopts the SIMPLE-C algorithm[26] to further study the impinging twin jet with cross-flow; the variations of pressure, velocity, turbulent kinetic energy and turbulent kinetic dissipation rate are closely related to the jet exit height above the ground surface, the nozzle space and the strength of cross-flow.

ANALYTIC STUDY

Assumptions

In order to simply the impinging twin jet with cross-flow ($RA = 0$–$0{\cdot}6$), the following assumptions are made.

1. The flow is a two-dimensional planar impinging twin jet only.
2. Both the upper plate surface and ground surface are adiabatic and the thermal effects on viscosity are not considered.

Governing equations

The general forms of the transport equation for the unsteady two-dimensional compressible impinging twin jet with and without cross-flow only differ with respect to the boundary conditions. The equation can be written as[27]

$$\frac{\partial(\rho\phi)}{\partial t}+\frac{\partial(\rho u\phi)}{\partial x}+\frac{\partial(\rho v\phi)}{\partial y}-\frac{\partial}{\partial x}\left(\Gamma_\phi\frac{\partial\phi}{\partial x}\right)-\frac{\partial}{\partial y}\left(\Gamma_\phi\frac{\partial\phi}{\partial y}\right)=S_\phi, \tag{1}$$

where the transfer coefficients Γ_ϕ, the source terms S_ϕ and the transport variables ϕ are as given in Table I. The total effective viscosity μ_e of the flow is

$$\mu_e=\mu_l+\mu_t,$$

where μ_l and μ_t are the molecular and eddy viscosity respectively; μ_t is known from the Jones–Launder k–ε two-equation turbulence model[10] as

$$\mu_t=C_\mu\rho k^2/\varepsilon.$$

NUMERICAL METHOD

The difficulty in solving the Navier–Stokes equations is that the non-linear and pressure terms are unknown. Patankar[28] initiated the SIMPLE algorithm to solve the main variables U, V and P. Van Doormaal and Raithby[26] and Chuang and Lii[29] showed that SIMPLE-C had a better

Table I. Governing equation variables[25]

ϕ	Γ	S	S_p/V	S_c/V
u	μ_e	$-\frac{\partial p}{\partial x}+S^u$	0	$S^u-\frac{\partial p}{\partial x}$
v	μ_e	$-\frac{\partial p}{\partial y}+S^v$	0	$S^v-\frac{\partial p}{\partial y}$
k	$\frac{\mu_e}{\sigma_k}$	$G-\rho\varepsilon$	$-\frac{C_\mu\rho^2 k}{\mu}$	G
ε	$\frac{\mu_e}{\sigma_\varepsilon}$	$\frac{C_1\varepsilon G-C_2\rho\varepsilon^2}{k}$	$-\frac{C_2\rho\varepsilon}{k}$	$\frac{C_1 G}{k}$

$C_1=1{\cdot}44,\quad C_2=1{\cdot}72,\quad C_\mu=0{\cdot}09,\quad \sigma_k=1{\cdot}0,\quad \sigma_\varepsilon=1{\cdot}3$

$$S^u=\frac{\partial}{\partial x}\left(\mu_e\frac{\partial u}{\partial x}\right)+\frac{\partial}{\partial y}\left(\mu_e\frac{\partial v}{\partial y}\right)-\frac{2}{3}\frac{\partial}{\partial x}\left[\mu_e\left(\frac{\partial u}{\partial x}+\frac{\partial v}{\partial y}\right)+\rho k\right]$$

$$S^v=\frac{\partial}{\partial x}\left(\mu_e\frac{\partial u}{\partial y}\right)+\frac{\partial}{\partial y}\left(\mu_e\frac{\partial v}{\partial y}\right)-\frac{2}{3}\frac{\partial}{\partial y}\left[\mu_e\left(\frac{\partial u}{\partial x}+\frac{\partial v}{\partial y}\right)+\rho k\right]$$

$$G=\mu_e\left\{2\left[\left(\frac{\partial u}{\partial x}\right)^2+\left(\frac{\partial v}{\partial y}\right)^2\right]+\left(\frac{\partial u}{\partial x}+\frac{\partial v}{\partial y}\right)^2\right\}$$

convergent residue mass rate than the SIMPLE algorithm. The present calculations were performed using the SIMPLE-C algorithm[26] and a power-law scheme.[28] TDMA and a line-by-line sweeping process at each time step iteration were utilized to calculate the non-linear governing finite difference equations.[25] Underrelaxation was used for each time step iteration to help convergence. The under-relaxation factors used in the present calculations are given in Table II.

Finite difference equations

Integration over the control volume cell was employed to construct the finite difference equations. First, the general form of equation (1) can be rewritten as

$$\frac{\partial(\rho\phi)}{\partial t}+\frac{\partial J_x}{\partial x}+\frac{\partial J_y}{\partial y}=S, \tag{2}$$

where

$$J_x=\rho u\phi-\Gamma\frac{\partial\phi}{\partial x}, \qquad J_y=\rho v\phi-\Gamma\frac{\partial\phi}{\partial y}.$$

Integration of equation (2) over the control volume gives

$$\iiint_V\left(\frac{\partial(\rho\phi)}{\partial t}+\frac{\partial J_x}{\partial x}+\frac{\partial J_y}{\partial y}\right)\mathrm{d}V=\iiint_V S\mathrm{d}V, \tag{3}$$

where $\mathrm{d}V=\mathrm{d}x\mathrm{d}y\mathrm{d}z=\mathrm{d}x\mathrm{d}y$. The finite difference equation for equation (3) with linearized source term is

$$\frac{(\rho_\mathrm{p}\phi_\mathrm{p}-\rho_\mathrm{p}^0\phi_\mathrm{p}^0)\Delta x\Delta y}{\Delta t}+J_\mathrm{e}-J_\mathrm{w}+J_\mathrm{n}-J_\mathrm{s}=(S_\mathrm{p}\phi_\mathrm{p}+S_\mathrm{c})\Delta x\Delta y, \tag{4}$$

where

$$J_i=\int J_x\mathrm{d}y\Big|_{\text{over interface } i} \quad (i=\mathrm{E},\mathrm{W}), \qquad J_i=\int J_y\mathrm{d}x\Big|_{\text{over interface } i} \quad (i=\mathrm{N},\mathrm{S}).$$

Also, integration of the continuity equation over the control volume cell gives

$$\frac{(\rho_\mathrm{p}-\rho_\mathrm{p}^0)\Delta x\Delta y}{\Delta t}+F_\mathrm{e}-F_\mathrm{w}+F_\mathrm{n}-F_\mathrm{s}=0. \tag{5}$$

Substracting equation (5) multiplied by ϕ_p from equation (4) gives

$$\rho_\mathrm{p}^0(\phi_\mathrm{p}-\phi_\mathrm{p}^0)\frac{\Delta x\Delta y}{\Delta t}+(J_\mathrm{e}-F_\mathrm{e}\phi_\mathrm{p})-(J_\mathrm{w}-F_\mathrm{w}\phi_\mathrm{p})+(J_\mathrm{n}-F_\mathrm{n}\phi_\mathrm{p})-(J_\mathrm{s}-F_\mathrm{s}\phi_\mathrm{p})=(S_\mathrm{p}\phi_\mathrm{p}+S_\mathrm{c})\Delta x\Delta y, \tag{6}$$

Table II. Underrelaxation factor f

	u	v	k	ε	P	μ_t
f	0·2	0·2	0·3	0·3	0·4	0·4

where F_i is the mass flow rate for surface i of the control volume. Then the total flux of the control volume cell can be written as

$$J_i - F_i\phi_p = a_i(\phi_p - \phi_i) \quad (i = E, N), \qquad J_i - F_i\phi_p = a_i(\phi_i - \phi_p) \quad (i = W, S), \tag{7}$$

where

$$a_i = D_i A(|P_i|) + [-F_i, 0] \quad (i = E, N), \qquad a_i = D_i A(|P_i|) + [F_i, 0] \quad (i = W, S),$$

$P_i = F_i/D_i$ is the Peclet number for surface i, $A(|P_i|)$ is a function of P_i and

$$D_i = \Gamma_i A_i/(\delta x)_i.$$

Substituting these relations in equation (6), we obtain

$$a_P\phi_P = a_E\phi_E + a_W\phi_W + a_S\phi_S + a_N\phi_N + b, \tag{8}$$

where

$$b = S_c\Delta x\Delta y + a_p^0\phi_p^0, \qquad a_p^0 = \rho_p^0\Delta x\Delta y/\Delta t, \qquad a_p = a_E + a_W + a_S + a_N + a_p^0 - S_p\Delta x\Delta y.$$

Details of the SIMPLE-C algorithm[25, 26] calculation procedures and the power-law scheme[28] will not be repeated here.

Initial value and boundary conditions

The initial value must be given for the time-marching method. The surrounding boundary conditions are given for the space-iterating method.

Initial value. The velocity, kinetic energy and dissipation rate of turbulence energy are zero except for the inlet condition and relative pressure.

Boundary conditions

(a) At the inlet.

$$V_i = (V_{in})_i \sin\theta_i \ (i = 1, 2), \ U_i = (V_{in})_i \cos\theta_i, \ k_i = 0{\cdot}003 \ (V_{in})_i^2$$

and

$$\varepsilon_i = C_\mu k_i^{3/2}/0{\cdot}03 \ (D_i/2).$$

(b) At the outlet. $\partial\phi/\partial X = 0$ and $V = 0$ ($\phi = u, k, \varepsilon, p$).

(c) At the wall. $U = 0$ and $V = 0$ (no-slip conditions), k and ε were handled by the wall function.[10, 27, 30]

(d) At the left hand with cross-flow: $U = RA(-1) \ (V_{in})_1$ (for cross-flow approach to right).

Grid system

A staggered grid[28] arrangement for integration over the control volume was used to avoid wavy phenomena. The arrangement of the grid system is shown in Figure 3.

(1) x-direction—non-uniform grid, expanding the stretching factor (RATIO) along both sides from the nozzle centres and the midpoint between the two nozzle exits, with RATIO = 1·05–1·25

(2) y-direction—uniform grid.

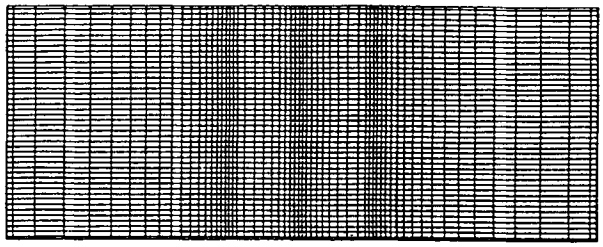

Figure 3. Staggered grid system of computation plane

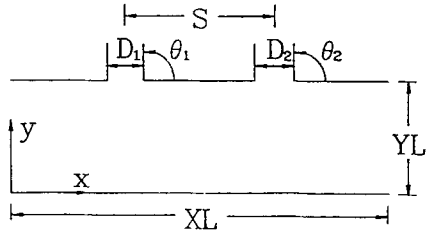

Figure 4. Geometry of physical plane

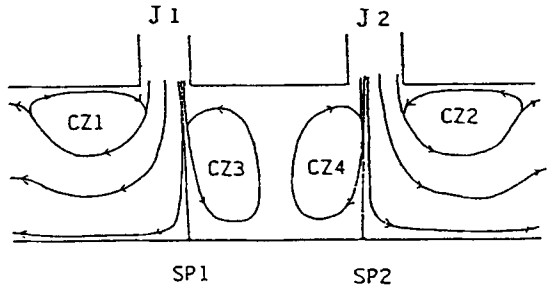

Figure 5. Configuration of impinging twin jet

RESULTS AND DISCUSSION

The flow fields of the impinging twin jet with an upper plate have been calculated in the present paper. The impinging twin-jet flow is a function of H, Re and RA. The geometry of the physical plane is shown in Figure 4. For this configuration the flow field model is fixed at $Re_1 = Re_2 = 13\,500$. The left-induced recirculation zone of nozzle J1 is called CZ1, the right-induced recirculation zone of nozzle J2 is called CZ2, the left recirculation zone below J1 and J2 is called CZ3, the right recirculation zone below J1 and J2 is called CZ4 and there are two stagnation points located in CZ3 and CZ4, called SP1 and SP2 respectively, as shown in Figure 5. The computed main velocity V of an impinging twin jet without cross-flow across the fountain flow for 64×46 grid points is shown in Figure 6 and found to have good agreement with the experimental data of Saripalli *et al.*[31] The calculated result for 64×46 grid points is close to that for 94×90 grid points as shown in Figure 6. Hence the 64×46 grid points selected in this paper to

simulate the impinging twin jet are reasonable. The contours of the flow variables (streamlines, normalized velocity U, velocity V, turbulent kinetic energy K, turbulent kinetic energy dissipation rate ε and static pressure P) of impinging twin-jet flow without cross-flow are shown in Figure 7.

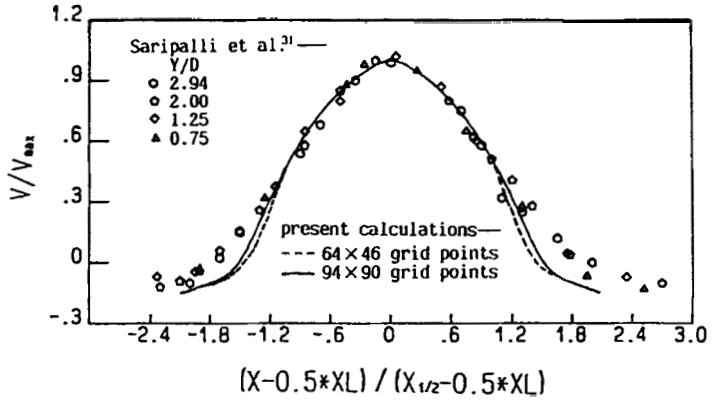

Figure 6. Mean velocity V across fountain flow ($YL/D=8$, $S/D=5$, $Re_1=Re_2=13\,500$)

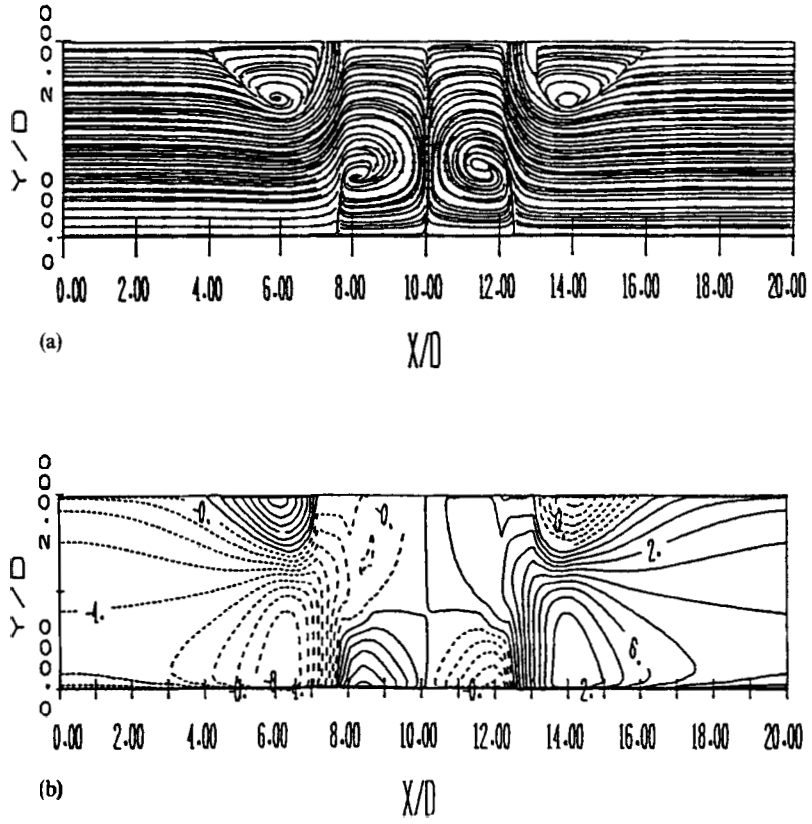

Figure 7. Primary flow variables for impinging twin jet without cross-flow ($H=1$, $RA=0$, $Re_1=Re_2=13\,500$): (a) streamlines; (b) normalized U; (c) normalized V; (d) normalized K; (e) normalized ε; (f) normalized P

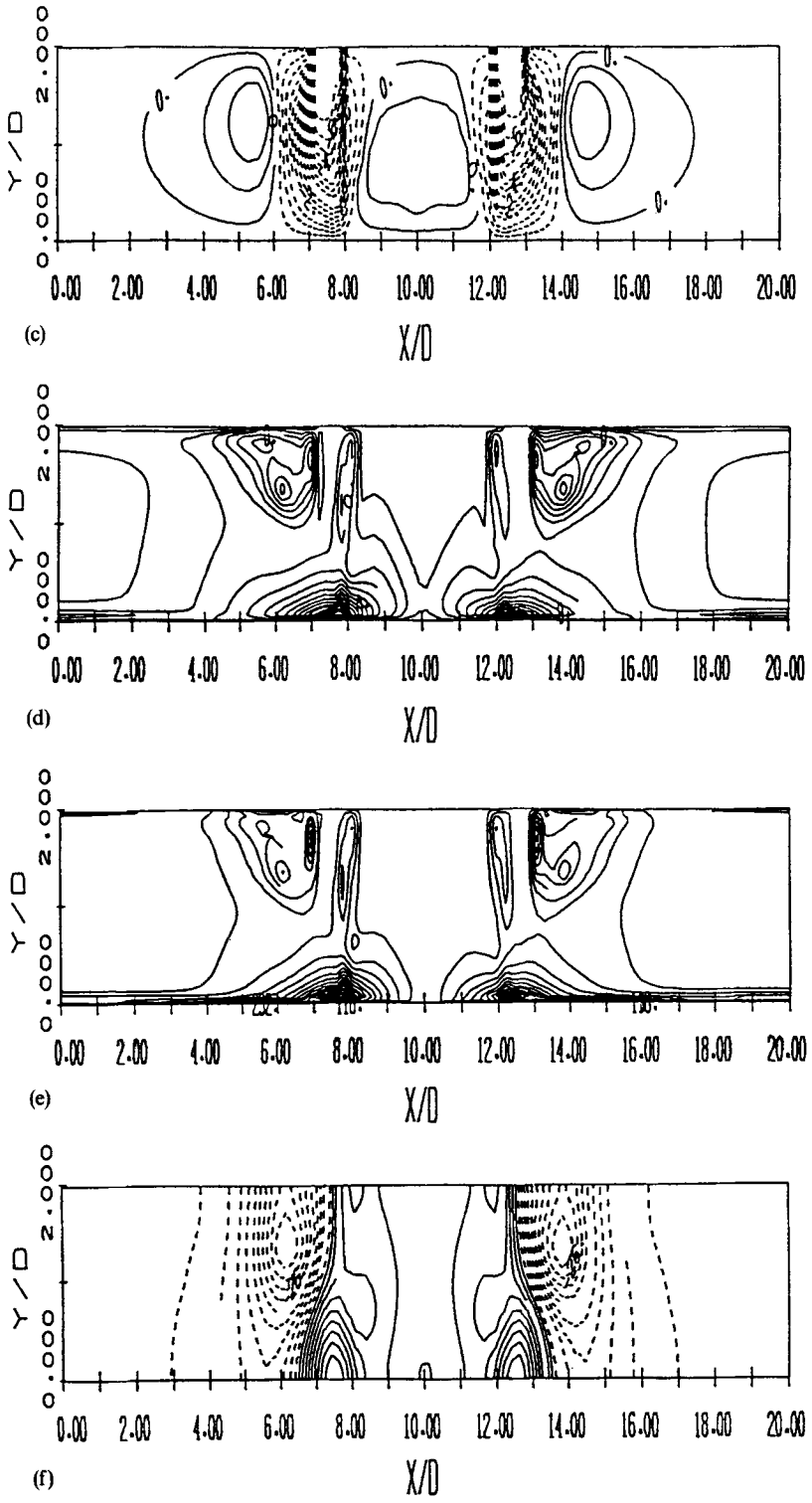

Figure 7. (Continued)

The contour plots of the primary flow variables as a function of RA (=0, 0·4) are shown in Figures 7 and 8. The cross-flow with $RA = 0{\cdot}4$ causes the flow direction of J1 to go to the right and destroys CZ1, CZ3 and CZ4, but forms a new recirculation zone (called CZ5) between J1 and J2, as shown in Figure 8. The maximum contours of K and ε are located near CZ2 because of the interaction of the inertia force of cross-flow and the viscous force of CZ2. The pressure is negative

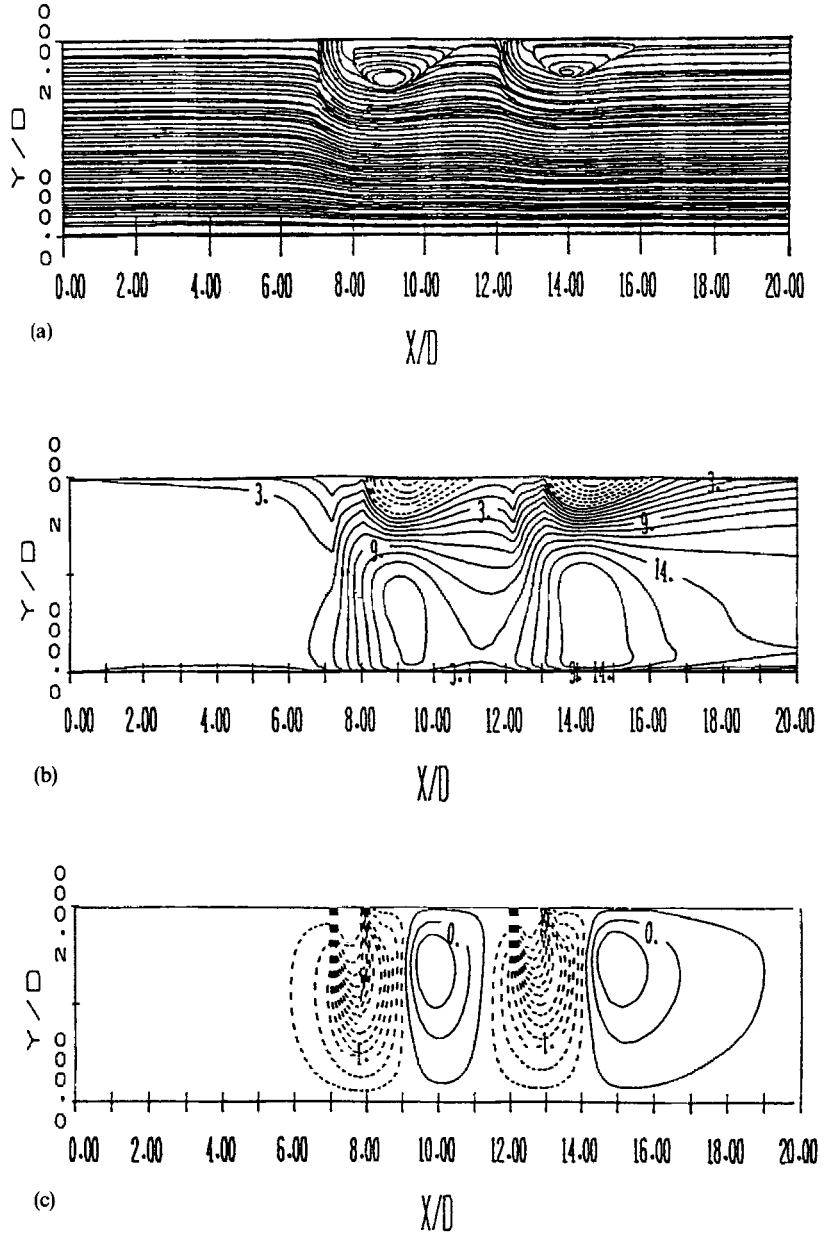

Figure 8. Primary flow variables for impinging twin jet with cross-flow ($H = 1$, $RA = 0{\cdot}4$, $Re_1 = Re_2 = 13\,500$): (a) streamlines; (b) normalized U; (c) normalized V; (d) normalized K; (e) normalized ε; (f) normalized P

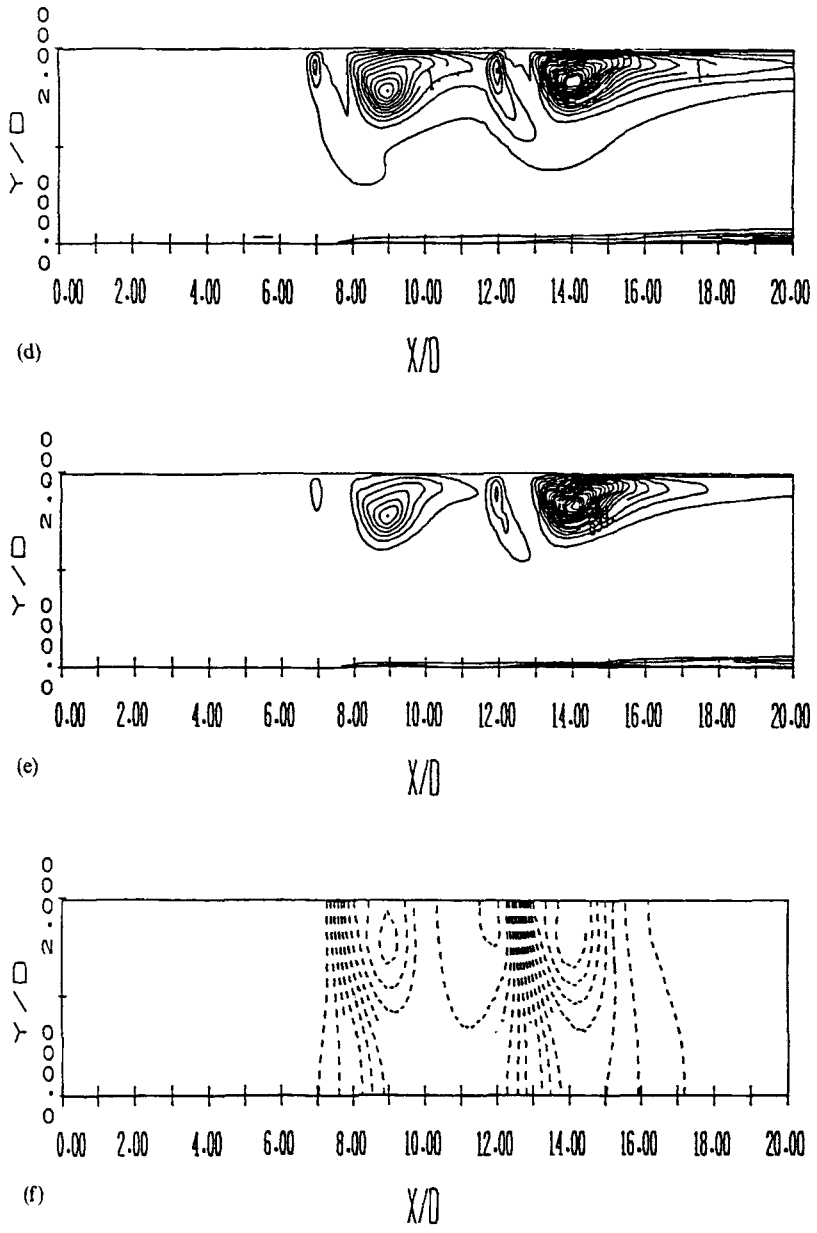

Figure 8. (Continued)

for all RA, as shown in Figure 8(f). The normalized pressure along the ground surface for $\theta_1 = \theta_2 = 90°$, $Re_1 = Re_2 = 13\,500$ and $YL/(D_1 + D_2) = 1$–6 is shown in Figure 9. From the present calculations the maximum pressure is located at the stagnation point. The pressure distributions are similar for $YL/(D_1 + D_2) = 1$ and 2. The stagnation point of flow is at about $X/XL = 0{\cdot}38$ and 0·62 for $YL/(D_1 + D_2) = 1$ and 2 respectively. The other smaller peak pressure between two

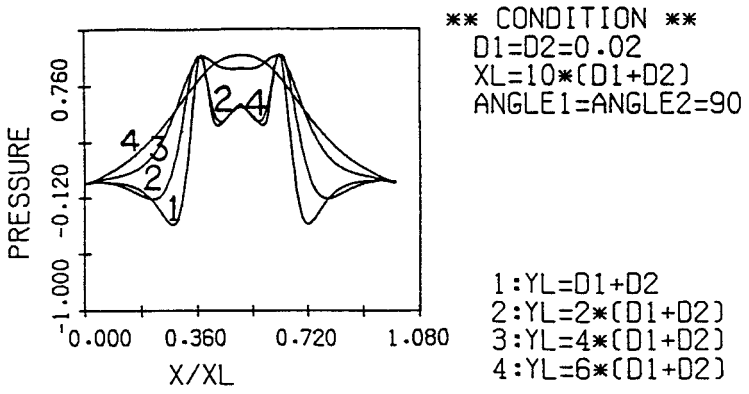

Figure 9. Pressure distribution of lower plate without cross-flow at different YL ($W=10$, $RA=0$, $Re_1=Re_2=13\,500$)

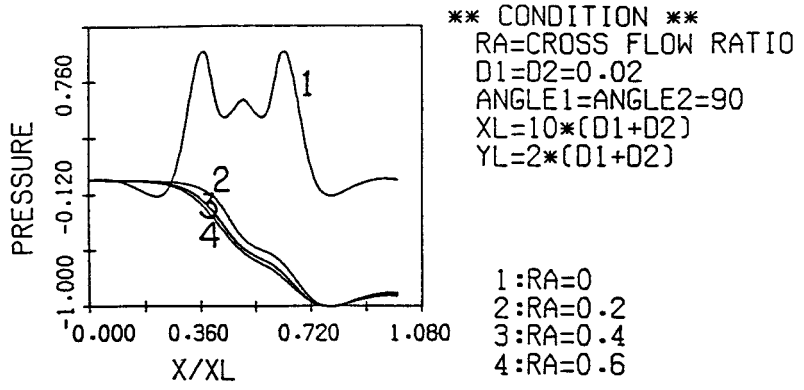

Figure 10(a). Pressure distribution of lower plate at different RA ($W=10$, $H=2$, $Re_1=Re_2=13\,500$)

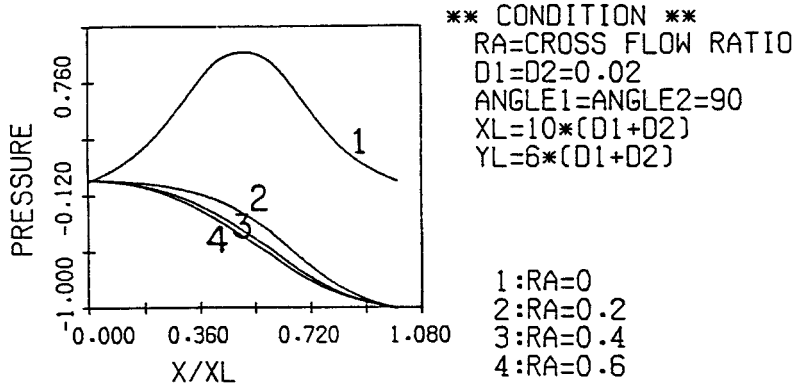

Figure 10(b). Pressure distribution of lower plate at different RA ($W=10$, $H=6$, $Re_1=Re_2=13\,500$)

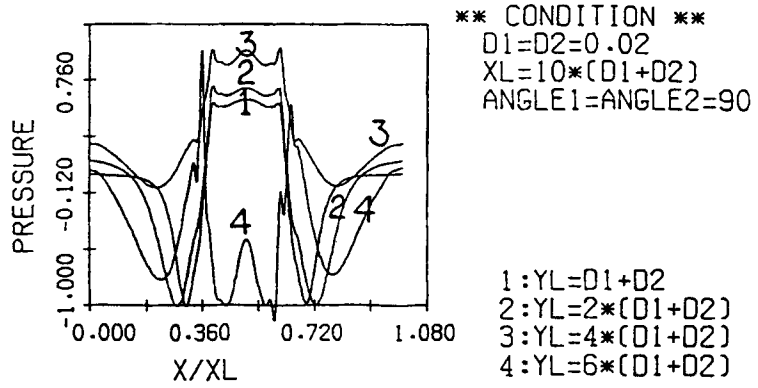

Figure 11. Pressure distribution of upper plate without cross-flow at different YL ($W=10$, $RA=0$, $Re_1=Re_2=13\,500$)

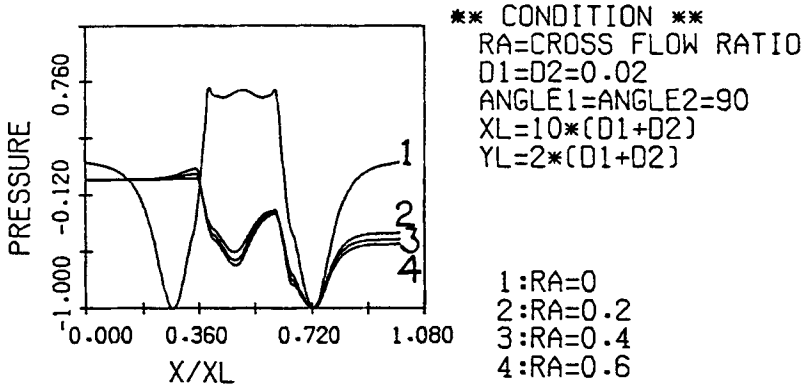

Figure 12(a). Pressure distribution of upper plate at different RA ($W=10$, $H=2$, $Re_1=Re_2=13\,500$)

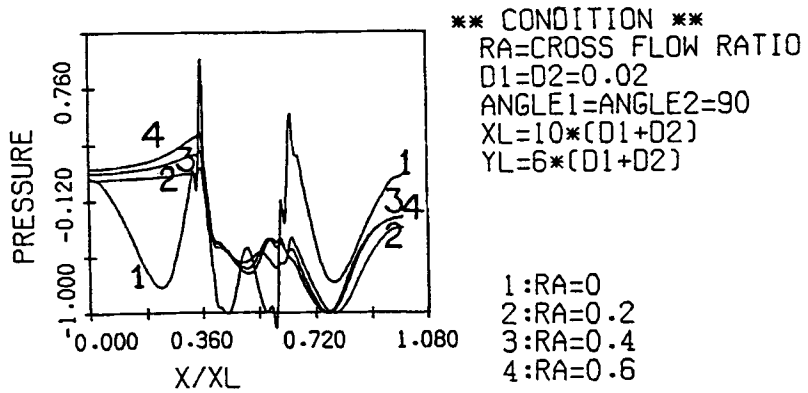

Figure 12(b). Pressure distribution of upper plate at different RA ($W=10$, $H=6$, $Re_1=Re_2=13\,500$)

stagnation points is due to the colliding wall jets. The profile of pressure distributions is bell-shaped and only one stagnation point is formed, due to a quasi-single jet impinging on the ground surface for $YL/(D_1+D_2)=6$. The peak pressure of the lower plate for impinging twin-jet flow without cross-flow is located at $X/XL=0{\cdot}38$ and $0{\cdot}62$ for SP1 and SP2 respectively, as shown in Figure 9. The location of the peak pressure is moved towards the right when RA is increased, as also shown in Figure 9. The pressure of the lower plate falls with increasing RA because the cross-flow makes the jet momentum of the nozzles flow to the right, as shown in Figures 10(a) and 10(b). The upper-plate pressure for impinging twin-jet flow without cross-flow is about the same with increasing H, as shown in Figure 11. Both CZ2 and CZ5 the low-pressure zones and the centres of CZ2 and CZ5 move to the right with increasing H for all RA, as shown in Figures 12(a) and 12(b). The centre of CZ5 moves a little to the right and the centre of CZ2 remains the same with increasing RA. A pressure jump of the upper plate on the left side of J1 occurs when RA is increased. This pressure jump phenomenon is due to the interaction between cross-flow and impinging jet flow. There is another recirculation zone (called CZ6) after CZ5 for $RA=0{\cdot}2$, as shown in Figures 13(a) and 13(c). This recirculation zone CZ6 dies out gradually with increasing RA, as indicated in Figures 13(a) and 13(b). The lift of the impinging twin jet decreases with increasing RA, as shown in Figure 14, but the lift increases when the height of the jet exit is increased.

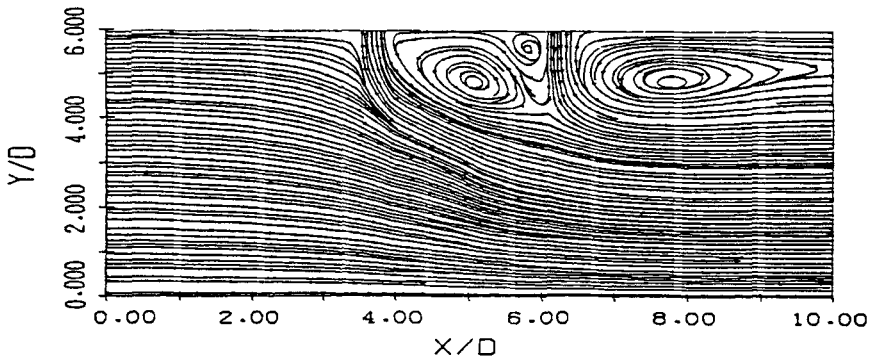

Figure 13(a). Streamlines of impinging twin jet with cross-flow ($H=6$, $RA=0{\cdot}2$, $Re_1=Re_2=13\,500$)

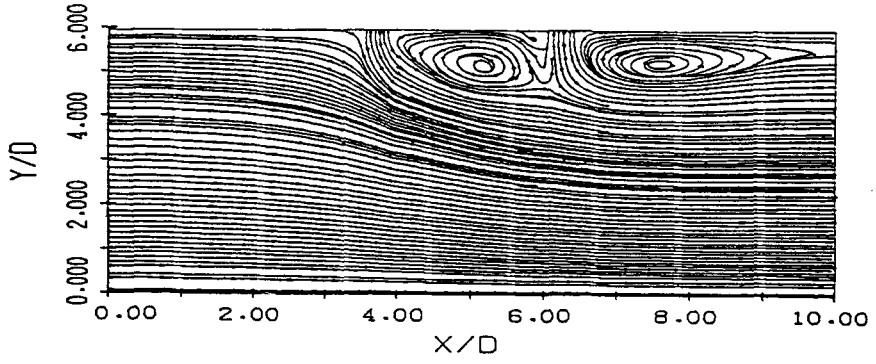

Figure 13(b). Streamlines of impinging twin jet with cross-flow ($H=6$, $RA=0{\cdot}4$, $Re_1=Re_2=13\,500$)

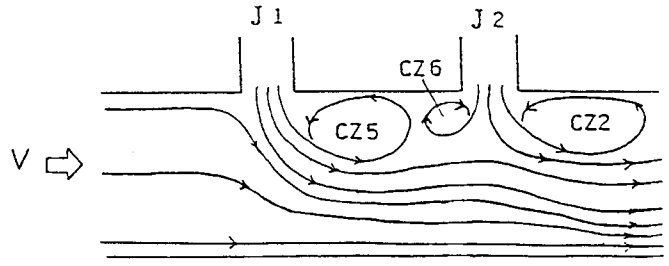

Figure 13(c). Schematic illustration of induced recirculation zones

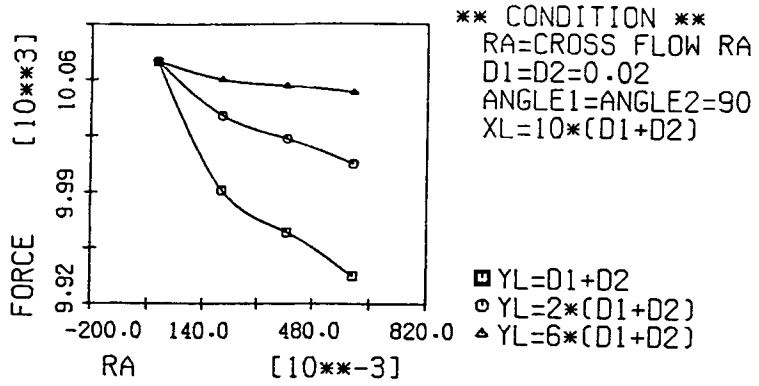

Figure 14. Variation of lift force of upper plate at different RA ($W=10$, $Re_1=Re_2=13\,500$)

CONCLUDING REMARKS

A theoretical study has been undertaken to determine the flow characteristics associated with a planar turbulent unsteady compressible impinging twin jet in ground effect. The principal emphasis has been on gaining an understanding of the interaction of the impinging twin-jet flow with cross-flow on a simulated fuselage undersurface.

The computed results show that RA has a strong influence on the pressure distributions of the lower and upper plates and on the lift of the flow. With the completion of a predictive scheme for the compressible impinging jet, the analysis will be extended to multiple-jet and three-dimensional flow problems. Such an analysis should provide more detailed insight into the propulsion-induced flows around V/STOL aircraft.

APPENDIX: NOMENCLATURE

A	area of control volume
C_1, C_2, C_μ	empirical constants in turbulence model
CZi	induced recirculation zone ($i=1-6$)
D_1, D_2	inlet width of exhaust nozzles ($D_1=D_2=D$)
H	normalized height of jet exit plane above ground ($=YL/(D_1+D_2)$)
Ji	nozzle ($i=1, 2$)
JR	normalized space of exhaust nozzles ($=S/(D_1+D_2)$)

K	kinetic energy
P	normalized static pressure $(=(P-P_{ref})/(P_s-P_{ref}))$
P_{ref}	static pressure of left outlet of lower plate
P_s	stagnation pressure of lower plate
RA	strength of cross-flow (=(velocity of cross-flow)/(inlet velocity of J1))
Re_i	Reynolds number $(=(V_{in})_i D_i/\mu,\ i=1, 2)$
SPi	stagnation point $(i=1, 2)$
S	source term of dependent variable
U	velocity component in x-direction
V	velocity component in y-direction
$(V_{in})_i$	exit velocity of nozzle $(i=1, 2)$
V_{max}	local maximum velocity in y-direction of fountain upwash flow
W	normalized width of solution domain $(=XL/(D_1+D_2))$
$X_{1/2}$	half-width of fountain flow, where $V=\frac{1}{2}V_{max}$
XL	length of lower or upper plate
YL	height of nozzle
Γ_ϕ	effective transfer coefficient for diffusion
μ_l	molecular viscosity
μ_e	effective viscosity
μ_t	turbulent viscosity
ε	turbulent kinetic energy dissipation rate

REFERENCES

1. M. Wolfshtein, 'Some solutions of the plane turbulent impinging jet', *J. Basic Eng., Trans. ASME*, **92d,** 915–922 (1970).
2. D. D. Coleman, 'A study of free jet impinging, Part I: Mean properties of free and impinging jets', *J. Fluid Mech.*, **45,** 281–319 (1971).
3. V. Parameswaran and S. A. Alpay, 'Normal impingement of jets', *J. Aircraft*, **11,** 189–191 (1974).
4. E. M. Sparrow and L. Lee, 'Analysis of flow field and impingement heat/mass transfer due to a nonuniform slot jet', *J. Heat Transfer ASME*, **67c,** 191–197 (1975).
5. M. J. Siclari, D. Migdal and J. L. Palcza, 'The development of theoretical models for jet-induced effects on V/STOL aircraft', *J. Aircraft*, **13,** 938–944 (1976).
6. W. W. Bower and D. R. Kotansky, 'A Navier–Stokes analysis of the two-dimensional ground effects problem', *AIAA Paper 76-621*, 1976.
7. W. W. Bower, D. R. Kotansky and G. H. Hoffman, 'Computations and measurements of two-dimensional turbulent jet impingement flowfields', *Symp. on Turbulent Shear Flows, Vol 1*, University Park, PA, 1977, pp. 3.1–3.8.
8. D. R. Kotansky and W. W. Bower, 'A basic study of the VTOL ground effect problem for planar flow', *J. Aircraft*, **15,** 214–221 (1978).
9. W. W. Bower, R. K. Agarwal and G. R. Peters, 'A theoretical study of two and three dimensional impinging jets', *MDRL 79-22*, 1979.
10. W. P. Jones and B. E. Launder, 'The prediction of laminarization with a two-equation model of turbulence', *Int. J. Heat Mass Transfer*, **15,** 301–314 (1972).
11. A. Rubel, 'Computations of jet impingement on a flat surface', *AIAA J.*, **18,** 168–175 (1980).
12. R. K. Agarwal and W. W. Bower, 'Navier–Stokes computations of turbulent compressible two-dimensional impinging jet flowfields', *AIAA J.*, **20,** 577–584 (1982)..
13. M. K. Looney and J. J. Walsh, 'Mean-flow and turbulent characteristics of free and impinging jet flows', *J. Fluid Mech.*, **147,** 397–429 (1984).
14. C. M. Ho and N. S. Nosseir, 'Dynamics of an impinging jet. Part 1. The feedback phenomenon', *J. Fluid Mech.*, **105,** 119–142 (1981).
15. D. Rockwell and A. Schachenmann, 'Self-generation and organized waves in an impinging turbulent jet at low Mach number', *J. Fluid Mech.*, **117,** 425–441 (1982).
16. C. M. Ho and N. S. Nosseir, 'Dynamics of an impinging jet. Part 1. The noise generation', *J. Fluid Mech.*, **116,** 379–391 (1982).
17. C. M. Ho and F. B. Hsiao, 'Evolution of coherent structure in a lip jet', *IUTAM Symposium on structure of Complex Turbulent Shear Flow*, Marseille, France, Spring-Verlag, 1982, pp. 121–136.

18. R. M. MacCormack, 'The effect of viscosity in hypervelocity impact cratering', *AIAA Paper 69-354*, 1969.
19. R. M. MacCormack, 'Computational efficiency achieved by time splitting of finite difference operators', *AIAA Paper 72-154*, 1972.
20. R. M. Beam and R. F. Warming, 'An implicit factored scheme for the compressible Navier–Stokes equations', *AIAA J.*, **16**, 393–402 (1978).
21. T. H. Pulliam and J. L. Steger, 'On implicit finite difference simulations of three dimensional flows', *AIAA Paper 78-10*, 1978.
22. C. J. Hwang and J. L. Liu, 'Numerical study of two-dimensional impinging jet flowfields', *AIAA J.*, **27**, 841–842 (1989).
23. R. M. MacCormack, 'A numerical method for solving the equations of compressible viscous flow', *AIAA Paper 81-0110*, 1981.
24. S. H. Chuang, 'Numerical simulation of an impinging jet on a flate plate', *Int. j. numer. methods fluids*, **9**, 1413–1426 (1989).
25. S. H. Chuang and C. Y. Wei, 'Computations of an oblique jet impingement on a flat surface', *Int. j. numer. methods fluids*, **12**, 637–653 (1991).
26. J. P. Van Doormaal and G. D. Raithby, 'Enhancements of the SIMPLE method for predicting incompressible fluids flows', *Numer. Heat Transfer*, **7**, 147–163 (1984).
27. D. G. Lilley, 'Primitive pressure–velocity code for the computation of strongly swirling flow', *AIAA J.*, **14**, 749–756 (1976).
28. S. V. Patankar, *Numerical Heat Transfer and Fluid Flow*, Hemisphere, New York, 1980.
29. S. H. Chuang and S. W. Lii, 'Combustion flowfield analysis of an afterburner with v-gutter flameholders', *Trans. ASSRC*, **21**, 39–54 (1988).
30. B. E. Launder and D. B. Spalding, 'The numerical computation of turbulent flows', *Comput. Methods Appl. Mech. Eng.*, **3**, 301–314 (1970).
31. K. R. Saripalli, J. C. Kroutil and J. R. Van Horn, 'Experimental investigation of Hover flowfields in water at the Mcdonnell Douglas Research Laboratories', *AGARD-CP-413*, 1986.